ARTICLE

GaN/NbN epitaxial semiconductor/superconductor heterostructures

Rusen Yan[1]*, Guru Khalsa[2]*, Suresh Vishwanath[1], Yimo Han[3], John Wright[2], Sergei Rouvimov[4], D. Scott Katzer[5], Neeraj Nepal[5], Brian P. Downey[5], David A. Muller[3,6], Huili G. Xing[1,2,6], David J. Meyer[5] & Debdeep Jena[1,2,6]

Epitaxy is a process by which a thin layer of one crystal is deposited in an ordered fashion onto a substrate crystal. The direct epitaxial growth of semiconductor heterostructures on top of crystalline superconductors has proved challenging. Here, however, we report the successful use of molecular beam epitaxy to grow and integrate niobium nitride (NbN)-based superconductors with the wide-bandgap family of semiconductors—silicon carbide, gallium nitride (GaN) and aluminium gallium nitride (AlGaN). We apply molecular beam epitaxy to grow an AlGaN/GaN quantum-well heterostructure directly on top of an ultrathin crystalline NbN superconductor. The resulting high-mobility, two-dimensional electron gas in the semiconductor exhibits quantum oscillations, and thus enables a semiconductor transistor—an electronic gain element— to be grown and fabricated directly on a crystalline superconductor. Using the epitaxial superconductor as the source load of the transistor, we observe in the transistor output characteristics a negative differential resistance—a feature often used in amplifiers and oscillators. Our demonstration of the direct epitaxial growth of high-quality semiconductor heterostructures and devices on crystalline nitride superconductors opens up the possibility of combining the macroscopic quantum effects of superconductors with the electronic, photonic and piezoelectric properties of the group III/nitride semiconductor family.

The experimental discovery[1] of superconductivity in 1911 predated the controllable synthesis and understanding of semiconductors[2] by nearly three decades. However, in the time it took to uncover the correlated physics behind superconductivity, rapid advances in the band-theory of semiconductors, perfection in crystal growth, and discoveries such as donor- and acceptor-doping and quantum heterostructure[3,4] design had unleashed their technological potential, enabling electronic amplifiers and switches, as well as light-emitting diodes and diode lasers that operate at room temperature. These solid-state devices have replaced bulky and slow vacuum tubes and table-top lasers, and have shrunk information processing, storage, and communication systems onto a chip.

Today, semiconductor transistors are reaching their fundamental Boltzmann limits in terms of switching energy and power consumption in the digital von-Neumann computational architecture[5], and communication systems are approaching their Shannon limits in terms of bandwidth and security. Quantum technologies have been envisaged to offer exponentially faster computation and guaranteed secure communications[6], and the leading materials for these emerging technologies make use of the macroscopic manifestation of quantum properties in superconductors. Devices such as Josephson junction flux qubits[7], lossless microwave resonators[8], AC Josephson junction lasers[9] and superconducting single-photon detectors[10] are the building blocks of these new quantum-information systems.

Substantial advances in such systems would be expected if the power of semiconductors could be combined with that of superconductors on a single epitaxial platform[11–13]. The group III/nitride semiconductors GaN (with a bandgap, E_g, of about 3.4 eV), indium nitride (InN; $E_g \approx 0.6$ eV) and AlN ($E_g \approx 6.2$ eV) constitute the most revolutionary semiconductor family since silicon. That is because they offer, in a single heterostructure material family (see Fig. 1), the necessary

ingredients for ultrafast microwave communications[14], ultralow-power computation[15], high-voltage switches[16], infrared through visible to deep-ultraviolet photonic emitters and detectors[17,18], and high-frequency circuit components such as surface acoustic wave and bulk acoustic wave filters[19]. On the other hand, one of the most technologically important superconductor families comprises the nitride compounds NbN_x, which have been used for superconducting radio-frequency circuits[20], squid magnetometers[21], Josephson junctions[22], single-photon detectors[10] for quantum communications and astronomy, and a host of other applications[23]. Here, we report the successful epitaxial integration of the semiconducting and superconducting nitride families as a crucial enabler for several applications.

Figure 1a shows that the lattice constants of Nb-based nitride metals— such as hexagonal Nb_2N and NbN, as well as cubic NbN rotated onto the (111) plane—are very close to the lattice constants of SiC, AlN and the GaN family. Wurtzite GaN and AlN can be grown on cubic (111) silicon, and hexagonal SiC serves as the substrate for the epitaxial growth of AlN- and GaN-based heterostructures for microwave transistors[24] and for quantum-well visible-light-emitting diodes[18]. Recently, we succeeded in growing crystalline epitaxial metal (epiMetal) niobium nitride layers by molecular beam epitaxy (MBE) on SiC, and further grew GaN and AlN layers on the epiMetal layers[25,26]. We found that the epiMetal layers retained high crystallinity and electronic conductivity down to thicknesses of a few nanometres[25,26]. The crystalline phases of the epilayers could be either hexagonal Nb_2N or NbN, or cubic NbN. In this study, we have determined that our films are cubic NbN_x, with x being around 0.75–0.88 as measured by secondary-ion mass spectrometry (SIMS). In what follows, we will simply refer to the phase and stoichiometry as NbN_x. The use of NbN_x enables an unprecedented level of epitaxial integration of buried metallic layers with wide-bandgap semiconductors and insulators.

[1]School of Electrical and Computer Engineering, Cornell University, Ithaca, New York 14853, USA. [2]Department of Materials Science and Engineering, Cornell University, Ithaca, New York 14853, USA. [3]School of Applied and Engineering Physics, Cornell University, Ithaca, New York 14853, USA. [4]Department of Electrical Engineering, University of Notre Dame, Indiana 46556, USA. [5]Electronics Science and Technology Division, US Naval Research Laboratory, Washington DC 20375, USA. [6]Kavli Institute for Nanoscale Science, Cornell University, Ithaca, New York 14853, USA. *These authors contributed equally to this work.
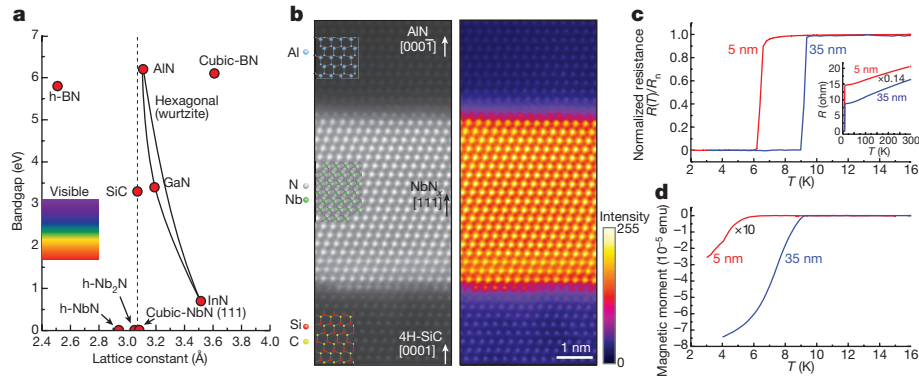
Figure 1 | Bandgap, lattice constant, crystallinity and superconductivity in epitaxial NbN_x on SiC. a, Bandgap versus lattice constant for select nitride semiconductors as well as for SiC. **b**, Cross-section HAADF-STEM images in black/white (left) and false-colour (right) of 5-nm NbN_x grown on an SiC substrate with a AlN capping layer. **c**, Resistance versus temperature (normalized to the resistance at 16 K), showing the superconducting phase transition of 5-nm (red) and 35-nm (blue) epitaxial NbN_x on SiC. Inset, resistance measured up to 300 K. **d**, The Meissner effect measured on the 5-nm and 35-nm samples, showing clear magnetic-flux expulsion accompanying the superconducting phase transition. These measurements are consistent with the T_c obtained in panel **c**. ×10 and ×0.14 indicate multiplication of the data by 10 or 0.14, respectively, to allow data of different scales to be shown on the same plot.

While investigating the low-temperature transport properties of the thin MBE-grown NbN_x layers, we find a superconducting phase transition at critical temperatures (T_c) ranging from 6 K to 15 K, similar to what has been found for NbN_x grown by other methods[27,28]. Epitaxial layers of NbN_x thinner than the coherence length are found to exhibit two-dimensional superconductivity, with in-plane critical magnetic fields ($H_c^{\parallel}$) well in excess of 20 T (the out-of-plane fields, $H_c^{\perp}$, are around 3 T). NbN_x is the first epitaxial superconductor to have been integrated with a technologically relevant semiconductor system.

Growth of NbN_x films by MBE

Niobium nitride used in superconducting electronics and bolometers for single-photon detectors, deposited by electron-beam evaporation or sputtering on non-epitaxial substrates, is typically polycrystalline[10,21]. Taking advantage of advances in MBE-based control of the growth of group III/nitride semiconductor heterostructures on SiC, we grew epitaxial layers of NbN_x directly on silicon-terminated, semi-insulating, four-hexagonal and six-hexagonal (4H and 6H) SiC substrates. We used a radio-frequency plasma nitrogen source of electronic-grade purity—identical to that used for AlN and GaN high-electron-mobility transistors (HEMTs), LEDs and lasers—to provide the active nitrogen atoms. We also used an electron-beam source of niobium, and monitored the growth *in situ* by reflection high-energy electron diffraction. Semiconducting Al(Ga)N/GaN quantum heterostructures were then grown epitaxially on top of the crystalline NbN_x layers.

Figure 1b shows high-angle annular dark-field scanning transmission electron microscopy (HAADF-STEM) images of 5 nm NbN_x epitaxial layers grown on a semi-insulating 4H-SiC substrate and capped with an AlN layer. The epitaxial NbN_x layers are nearly completely cubic, with high crystalline quality over large areas. Occasional twin boundaries are seen—typically separated by about 1 μm—as would be expected from the symmetry mismatch between cubic NbN_x and hexagonal SiC and AlN (see Extended Data Fig. 1). Figure 1b shows the epitaxial AlN on the NbN_x to be of nitrogen polarity; the entire AlN layer and all subsequent nitride semiconducting layers are hexagonal. The surfaces of uncapped NbN_x layers were extremely smooth, with a root-mean-square surface roughness of 0.16 nm for a 1 μm × 1 μm region, as measured by atomic force microscopy (AFM; see Extended Data Fig. 2). Extended Data Fig. 3 shows X-ray diffraction (XRD) images of the epitaxial NbN_x.

Electronic and magnetic properties of MBE-grown NbN_x

In its normal state we find that MBE NbN_x films are metallic with a resistivity of about 10^{-5} Ω cm, comparable to that of bulk platinum at room temperature. The measured Hall-effect carrier sign is negative, indicating electron conductivity, and the Hall-effect carrier density in three dimensions (n_{3d}) is about 2×10^{23} cm^{-3}, with a mean free path (λ) of roughly $1 - 2a_0$, where a_0 is the lattice constant (see Extended Data Table 1 for more metallic-state properties). Using a spherical Fermi surface approximation, the Mott–Ioffe–Regel criterion indicates that $k_F\lambda$ is much greater than 1, where the Fermi wavevector (k_F) is about $(3\pi^2 n_{3d})^{\frac{1}{3}}$, implying that the normal state transport is far above the minimum metallic conductivity regime. Although the Fermi surface is not spherical, we expect this conclusion to hold. We therefore find that our epitaxial NbN_x films are best characterized as working in the dirty limit ($\lambda \ll \xi$, where ξ is the coherence length), where the electron mean-free path is less than the Cooper-pair coherence length extracted from superconducting measurements, as described next.

Electrical transport measurements performed on the NbN_x layers, for thicknesses ranging from 4 nm to 100 nm, revealed superconductivity at transition temperatures of between 6 K and 15 K. Figure 1c shows the measured resistance $R(T)$ normalized to the resistance at 16 K (R_n) for NbN_x layers of thickness 5 nm and 35 nm. The resistivity of the samples exhibits a superconducting phase transition at around 7 K for the 5-nm sample, and about 9 K for the 35-nm sample. The inset shows the resistance up to 300 K for these two samples. In the metallic phase for temperatures $T_c < T < 300$ K, the resistance shows an expected increase owing to phonon scattering. Figure 1d shows the Meissner effect measured on these two samples by vibrating sample magnetometry (VSM), revealing clear magnetic-flux expulsion accompanying the superconducting phase transition. The superconductivity transition temperature measured from electron transport and the Meissner effect are found to be consistent.

When the thickness of the semiconductor heterostructure quantum wells becomes smaller than the electron de-Broglie wavelength, quantum confinement drives signature two-dimensional effects such as the integer quantum Hall effect in single-particle magnetotransport[29]. Similarly, when the thickness of a superconducting layer d is less than the coherence length ξ, a high anisotropy in the Meissner effect upper critical field $H_c^{\parallel}$ versus $H_c^{\perp}$ is expected. These effects were recently reported in monolayer $NbSe_2$, a transition-metal dichalcogenide superconductor[30]. Figure 2a, b shows the out-of-plane and in-plane magnetic-field-dependent normalized resistance $R(T)/R_n$ as a function of temperature for the 35-nm NbN_x epitaxial film. The variation of the critical field with the critical temperature is shown in Fig. 2c. Both out-of-plane and in-plane magnetic fields of strengths 0–4 T are seen to lower the critical temperature approximately linearly.
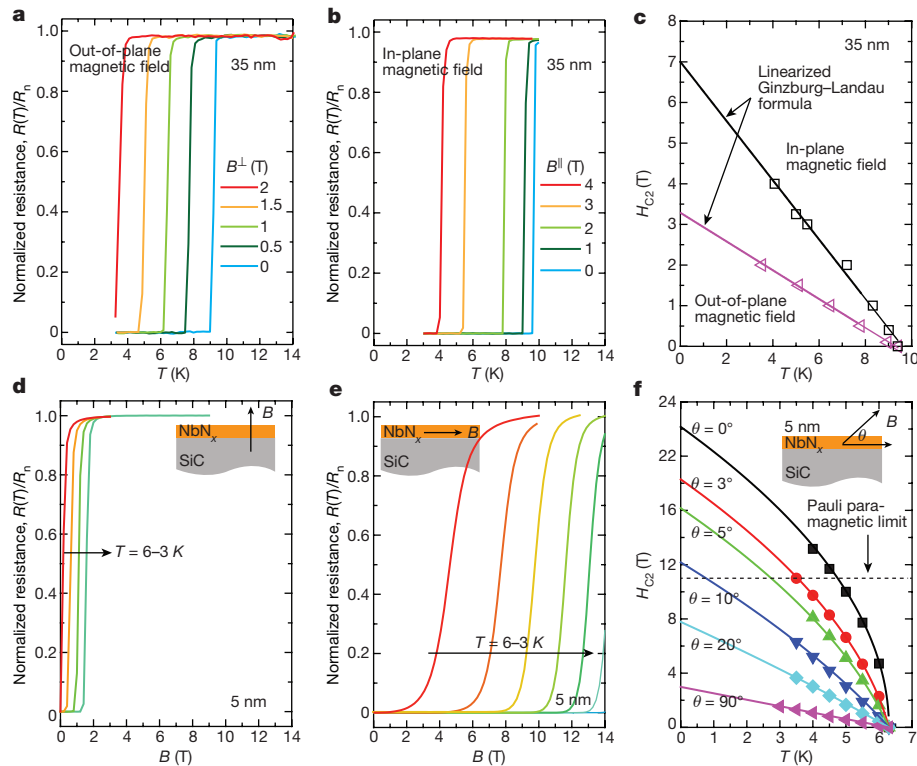
Figure 2 | Magnetotransport measurements on 35-nm and 5-nm NbN$_x$ epitaxial films, showing two-dimensional superconductivity when the epilayer thickness is less than the coherence length. a–c, 35-nm NbN$_x$ films. d–f, 5-nm NbN$_x$ films. a, b, Temperature-dependent normalized resistance for the 35-nm sample, for various out-of-plane magnetic fields $B^{\perp}$ (a) and in-plane fields $B^{\parallel}$ (b). c, The critical field H_{c2} decreases linearly with temperature, consistent with the Ginzburg–Landau model of bulk superconductivity. d, For the 5-nm NbN$_x$ sample, the out-of-plane magnetic field destroys superconductivity easily at low fields. e, Much higher critical fields are needed when the field is in-plane. f, This strong anisotropy of critical fields is shown, plotting the critical field H_{c2} versus temperature for various angles, θ, made by the magnetic field with the NbN$_x$ plane. The lines fit the linearized Ginzburg–Landau formula at $\theta = 0°$ and $\theta = 90°$, and the lines for the intermediate angles are consistent with the Tinkham formula (see text).

The behaviour of the 5-nm-thick NbN$_x$ epitaxial layer is quite different. Figure 2d, e shows that substantially stronger in-plane magnetic fields compared with out-of-plane fields are required to break superconductivity for the 5-nm sample. The 5-nm sample remains superconducting at 3 K for in-plane fields up to 14 T, whereas the 35-nm sample is far into the metallic regime at this field.

The linearized Ginzburg–Landau equation for the perpendicular critical field is:

$$H_{c2}^{\perp}(T) = \frac{\phi_0}{2\pi\xi^2}\left(1 - \frac{T}{T_c}\right) \qquad (1)$$

where $\phi_0 = h/2e$ is the superconducting flux quantum, with h being the Planck constant and $2e$ the charge of a Cooper pair; and $\xi = \xi_{GL}(0)$ is the extrapolation of the Ginzburg–Landau coherence length to $T = 0$ K. From the $\theta = 90°$ fits in Fig. 2c, f, we extract $\xi \approx 11$ nm for the $d = 5$-nm sample, and $\xi \approx 10$ nm for the $d = 35$-nm sample. This explains our choice of representative sample thicknesses: one sample behaves like a thin film ($d > \xi$) and one is in the two-dimensional limit ($d < \xi$).

When the film thickness d is less than ξ, vortex formation under an in-plane magnetic field is severely suppressed. Because the density of Cooper pairs cannot change on a length scale shorter than ξ, vortices cannot accommodate flux for in-plane magnetic fields. Because for the $d = 5$-nm film $d \leq \xi/2$, Cooper-pair breaking caused by orbital effects requires a higher in-plane than out-of-plane magnetic field to destroy superconductivity. We believe that the Zeeman effect for pair-breaking[31] is suppressed in our NbN$_x$ films, and that orbital-pair-breaking is the dominant mechanism responsible for the abnormally large $H_{c2}^{\parallel}$ values. For in-plane critical fields, the Ginzburg–Landau formula in the two-dimensional limit is:

$$H_{c2}^{\parallel}(T) = \frac{\sqrt{12}\,\phi_0}{2\pi\xi d}\left(1 - \frac{T}{T_c}\right)^{\frac{1}{2}} \qquad (2)$$

With ξ extracted from equation (1), the effective superconducting thickness is extracted to be $d = 4.9$ nm for the thin NbN$_x$ layer, in excellent agreement with the thickness measured by STEM. The extrapolation of this formula for $\theta = 0°$ in Fig. 2f to $T \to 0$ K suggests an upper critical field $H_{c2}^{\parallel}$ of about 22 T. This is twice the value of the Pauli paramagnetic limit, H_p, of about $1.86 \times T_c$—that is, 11 T—resulting from the Bardeen–Cooper–Schrieffer theory of superconductivity[31]. Such behaviour has also been observed in ultrathin superconducting systems: atomically thin layered transition-metal dichalcogenides[30], ultrathin metals[32] and oxide heterojunctions[33] have all shown an anomalously large $H_{c2}^{\parallel}$. The possible reasons for this phenomenon are discussed further in the Methods.

We further ascertained the importance of the orbital-pair-breaking effect rather than the Zeeman effect by measuring the angle-dependent critical field for the thin NbN$_x$ sample. The results of angle-dependent magnetotransport measurements at $\theta = 0°$, 3°, 5°, 10°, 20° and 90° for the 5-nm sample are shown in the H_{c2} versus T_c phase diagram in Fig. 2f; θ is the angle that the magnetic-field vector makes with the NbN$_x$/SiC heterointerface. The critical-field dependence on temperature changes from linear for $\theta = 90°$ to strongly nonlinear for $\theta = 0°$ for the 5-nm sample, whereas it remains linear for the 35-nm sample. As shown in Fig. 2f, the experimentally measured H_{c2} versus T_c at

intermediate angles at $\theta = 3°$, 5°, 10° and 20° shows an exceptional agreement with the Tinkham formula[34,35]:

$$\left| \frac{H_{c2}(\theta, T)\sin\theta}{H_{c2}^{\perp}(T)} \right| + \left(\frac{H_{c2}(\theta, T)\cos\theta}{H_{c2}^{\parallel}(T)} \right)^2 = 1 \qquad (3)$$

where $H_{c2}^{\perp}(T)$ and $H_{c2}^{\parallel}(T)$ are obtained from equations (1) and (2), and thus $H_{c2}(\theta, T)$ is obtained by solving equation (3). Given that the Tinkham formula is obtained purely from the coupling between electron momentum and magnetic field[34], the close agreement indicates that the observed pair-breaking is primarily a result of orbital effects, instead of the Zeeman effect (see Methods for further discussion). With the experimental determination of the critical temperature, coherence length and critical fields complete, we moved to the integration of nitride semiconductor heterostructures with epitaxial NbN$_x$ films.

Semiconductor/superconductor heterojunctions

The ability to grow epitaxial Al(Ga)N and GaN on NbN$_x$ has created an opportunity for the intimate integration of semiconductors with superconductors. To demonstrate this functionality, we have grown a GaN/AlGaN quantum-well heterostructure on the buried epitaxial NbN$_x$ superconducting layer, as shown in Fig. 3a. After epitaxial growth of 28-nm NbN$_x$ on SiC, a 22-nm AlN layer, a 1.3-μm GaN buffer layer, a 32-nm Al$_{0.4}$Ga$_{0.6}$N barrier, and a 32-nm GaN channel layer are grown successively by MBE in a single run without breaking vacuum. The entire AlN/GaN/AlGaN/GaN heterostructure takes a nitrogen-polar wurtzite form of high crystallinity and has a sharp heterojunction. This is confirmed by Hall-effect measurements of the mobility (μ) of a two-dimensional electron gas (2DEG) of about 1,350 cm^{2}V^{-1}s^{-1} at 300 K and about 3,400 cm^{2}V^{-1}s^{-1} at 2 K, with two-dimensional densities (n_{2d}) of about 1.3×10^{13} cm^{-2} at 300 K and 1.2×10^{13} cm^{-2} at 2 K. The 2DEG is formed in a triangular quantum well that is produced at the top GaN/Al$_{0.4}$Ga$_{0.6}$N heterojunction owing to the Berry-phase-driven spontaneous and piezoelectric polarization difference between AlGaN and GaN[36]. The high 2DEG mobility is comparable to that obtained in similar heterostructures without the NbN$_x$ buried layer, indicating a successful epitaxial integration. The Hall-effect measurement also proves that the 2DEG is electrically isolated from the buried NbN$_x$ metal layer. This 2DEG channel has enabled the integration of
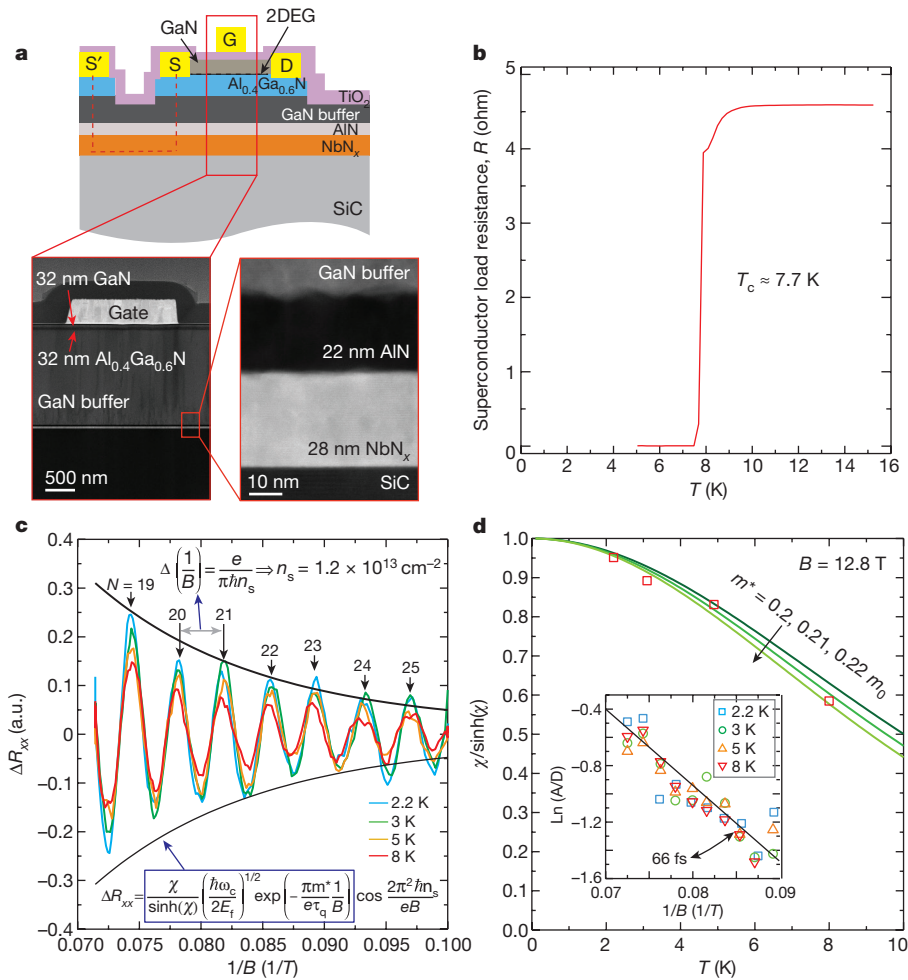

Figure 3 | Electrical and magnetotransport characterizations of group III/nitride/NbN$_x$ heterostructures. a, Cross-section schematic (top) and scanning transmission electron microscopy (STEM) imaging (bottom left and right) of Al(Ga)N/GaN HEMTs/NbN$_x$ grown by MBE on SiC substrates. **b**, Four-probe resistance of the buried epitaxial NbN$_x$ layer, showing that it remains superconducting—with a T_c of about 7.7 K—after the subsequent growth of the HEMT. **c**, Measured ΔR_{xx} versus $1/B$ at various temperatures, extracted from the longitudinal resistivity (R_{xx}) versus $1/B$ after background subtraction (see Methods). The resistance oscillation period, $\Delta(1/B)$, is 0.0038 T − 1, which can be used to estimate

carrier concentration as ns $= 1.26 \times 10$ cm^{-2}. The numbers on the arrows indicate the Landau level indices. **d**, $\chi/\sinh(\chi)$ as a function of temperature at $B = 12.8$ T. The lines are fittings made using effective masses, m^*, of 0.2 m_e, 0.21 m_e and 0.22 m_e. The inset shows Dingle plots at various temperatures, allowing extraction of the quantum-scattering time τ_q. The linear fit to experimental data gives $\tau_q = 66$ fs, which translates to a momentum/quantum-scattering ratio of $\tau_t/\tau_q = 5.6 >> 1$—a clear indication of charged dislocations as the dominant scattering mechanism in this 2DEG[42].

an HEMT with NbN_x; before describing this integration, we discuss the quantum-transport properties of the 2DEG channel as probed by low-temperature magnetoresistance.

Low-temperature and high-magnetic-field measurements revealed clear Shubnikov–de Haas oscillations in the magnetoresistance of the 2DEG (Fig. 3c, d). These oscillations are commensurate with the magnetic-field-driven formation of Landau levels, and are used to extract the carrier concentration, electron effective mass, and quantum-scattering times[37,38] by using the Lifshitz–Kosevich[39] form of the magnetoresistance:

$$\Delta\rho \propto \mathcal{R}_T \mathcal{R}_D \cos\left(\frac{2\pi^2 \hbar n_{SdH}}{eB}\right)$$

In this equation, the periodicity in inverse magnetic field depends only on the carrier concentration n_{SdH} and the fundamental constants e and $\hbar$. The measured period of $\Delta(1/B) = 0.0038$ T^{-1} shown in Fig. 3c corresponds to a carrier concentration of 1.26×10^{13} cm^{-2}, consistent with low-field Hall-effect measurements. $\mathcal{R}_T = \chi/\sinh(\chi)$ measures the thermal damping owing to a broadening of Landau levels, with the dimensionless factor $\chi = 2\pi^2 k_B T/\hbar\omega_c$ parametrizing the ratio of the thermal energy to the Landau-level energy separation[39]. Here k_B is the Boltzmann constant, T is the temperature, and $\omega_c = eB/m^\star$ is the cyclotron frequency with effective mass $m^\star$. Figure 3d shows the factor $\mathcal{R}_T$ plotted against the temperature dependence of the $N = 19$ Landau-level peak amplitude. The effective mass $m^\star \approx 0.21 m_e$ extracted from this plot is consistent with prior reports for 2DEGs in GaN[40]. Using the measured effective mass, the Dingle factor $\mathcal{R}_D = \pi m^\star/e\tau_q B$ reveals the quantum-scattering lifetime τ_q (ref. 41). The inset of Fig. 3d shows that the peak amplitude varies with inverse magnetic field for various temperatures with a characteristic quantum-scattering time of about 66 fs. This value is substantially smaller than the transport-scattering time (τ_t) extracted from the low-temperature Hall-mobility measurement; the ratio $\tau_t/\tau_q = 5.6$, being much greater than 1, suggests that Coulomb scattering from charged dislocations is the dominant scattering mechanism in the 2DEG[42]. Dislocations of density of about 10^9 cm^{-2} are typically present in GaN/AlGaN 2DEGs grown on SiC, Si or other substrates[42–44]. We emphasize that the presence of magnetic quantum oscillations demonstrates the high-quality epitaxial growth of the GaN/AlGaN 2DEG on the superconducting NbN_x film.

We fabricated nitrogen-polar GaN HEMTs as described in ref. 26. Low-resistance source/drain ohmic contacts were formed to the polarization-induced 2DEG, and 10 nm TiO_2 high-K dielectric was used before depositing the gate metal. Details of the process and device dimensions are described in the Methods. To form an electrical contact to the NbN_x layer, we applied a large voltage between two adjacent metal contacts, S and S′, that were initially isolated from each other by mesa etching (Fig. 3a). This process formed a low-resistance contact between S and S′ through the epitaxial NbN_x layer (dashed red line in Fig. 3a). A four-probe resistance measurement on such contacts (see Fig. 3b and Methods) confirmed that the buried NbN_x epilayer retained its superconductivity, with a transition temperature of around 7.7 K, even after the epitaxial growth of the entire nitride heterostructure on top of it and the subsequent device processing and annealing steps.

Figure 4a shows the HEMT drain current (J_d) per unit width, $J_d = I_d/W$, in logarithmic scale as a function of the gate voltage for two drain voltages at 5 K. Note that the gate voltage $V_{gs′}$ (the voltage difference between gate g and source s′) and drain voltage $V_{ds′}$ (the voltage difference between drain d and source s′) are measured with the buried NbN_x layer serving as the source load of the HEMT. The gate leakage current is low, and the drain current changes by about six to seven orders of magnitude as the Fermi level of the GaN quantum-well channel is pulled from inside the conduction band at $V_{gs′} = 0$ V into the gap at $V_{gs′} = -8$ V. The high on/off ratio was also observed at room temperature, as shown in Extended Data Fig. 4 and discussed in the Methods.

To quantify the effect of the superconducting load element, we compare the current in the HEMT from the drain (D) to S and S′ under varying gate voltages. The J_d–V_{gs} transfer curve measured at 5 K deviates from the J_d–$V_{gs′}$ transfer curve for currents of greater than 0.1 A mm^{-1} (Extended Data Fig. 5). Below 0.1 A mm^{-1}, NbN_x remains superconducting with $R_{sc} = 0$ Ω, and therefore does not contribute to the measured transfer curve. A current larger than 0.1 A mm^{-1} drives the NbN_x into a normal metal state with $R_{sc} \approx 4.6$ Ω. The superconductor-to-metal phase transition can occur when the magnetic field is greater than the critical magnetic field (H_c), when the current density is higher than the critical current density (J_c), or when the temperature is higher than the critical temperature (T_c). According to Ampere's law, the magnetic field resulting from the 2DEG current J_d at the superconducting layer is around $\mu_0 J_d/2 \approx 10^{-4}$ T (that is, much less than H_c). As shown in Extended Data Fig. 6, we have measured the critical current density of the MBE NbN_x to be $J_c = 10^5$ A cm^{-2}, and for a thickness of $t = 28$ nm the net current density is estimated to be $J = 10^3$ A cm^{-2} (much less than J_c). Thus, we rule out the Meissner effect and high current injection as possible causes of the superconductor-to-metal transition driven by the transistor. We attribute the transition to Joule heating at the semiconductor/superconductor junction. The abrupt appearance of a resistive load lowers the measured transistor current flowing across D-to-S′, changing the transfer curve. Further investigation of this electronic phase change in the load shows that the effect is strong enough to drive a negative differential resistance (NDR) in the transistor output characteristics.

Figure 4b–d shows the measured J_d–$V_{ds′}$ output characteristics of the HEMT as a function of gate voltages, measured at 10 K, 7 K and 5 K, with the NbN_x layer as the source load. At temperatures of 10 K (greater than T_c), the NbN_x layer acts as a resistive load at all bias conditions, and J_d increases monotonically with $V_{ds′}$ (Fig. 4b). As the temperature is lowered to 7 K (less than T_c), the NbN_x load drops to its zero-resistance state. This is characterized by a lower transistor on-resistance and a weak NDR (Fig. 4c).

As the power level is increased, Joule heating warms the NbN_x/AlN/GaN junction to temperatures higher than T_c, turning the surrounding superconducting NbN_x into a normal metal, and thus lowering the channel current. The abrupt increase in resistance caused by the superconductor-to-metal transition leads directly to the appearance of an NDR, as seen clearly seen in Fig. 4c, d. The transition regime of load from superconducting phase to normal metal for all J_d–$V_{ds′}$ curves at 7 K and 5 K lies within two iso-power contours, $P = I \times V$ (solid and dashed lines in Fig. 4c, d). This is a clear indication that the phase transition is thermally induced by Joule heating, and not through the critical current or critical magnetic field of NbN_x. A critical-current-mediated manifestation or a critical-magnetic-field-mediated phase transition would have caused an NDR at the same current level, not the same power level.

This form of a phase-transition element attached at the source contact of a transistor has been used to demonstrate sub-Boltzmann switching in silicon and GaN transistors at room temperature[45]. In such phase-field-effect transistors, the phase change was obtained through a filamentary metal-to-insulator transition in VO_2 that was driven through a combination of thermal phase transition and Mott–Hubbard interactions by injected current. The superconducting phase transition at a low temperature in the hybrid superconductor–transistor phase-field-effect transistors and the resulting NDR behaviour has not been observed before.

Conclusions

The successful epitaxial integration of group III/nitride semiconductors and transistor gain elements with NbN_x-based superconductors points towards several new opportunities. Just as the development of reduced surface and interface states of silicon paved the way for the metal-oxide-semiconductor field-effect transistor, so do epitaxial NbN_x/group III/nitride structures offer the possibility of defect-free metal/semiconductor heterojunctions. Semiconductor transistors were

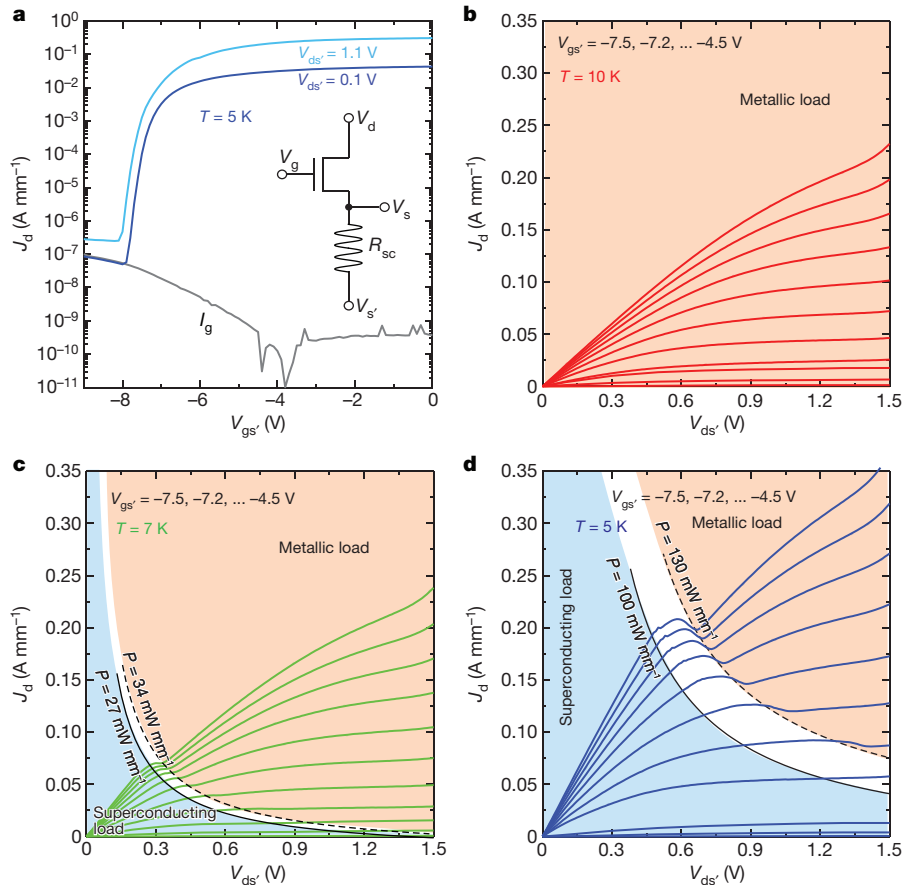**Figure 4 | Current–voltage characterizations of HEMTs with a superconducting source load at low temperatures. a**, Drain current density versus gate–source voltage (J_d–$V_{gs'}$) transfer curves of the HEMTs at 5 K, showing a high on/off ratio at $V_{ds'} = 0.1$ V and 1.1 V. The inset shows the equivalent circuit diagram for the device. **b–d**, J_d, versus source–drain voltage, $V_{ds'}$, for various top-gate voltages, $V_{gs'}$, of GaN HEMTs with a buried epitaxial superconductor load at the source side, at temperatures of 10 K (**b**), 7 K (**c**), and 5 K (**d**). The results show that when the NbN$_x$ layer becomes superconducting, the transistor output characteristics exhibit a negative differential resistance (NDR), as seen by the decrease in resistance with increasing $V_{ds'}$ between the iso-power contours. The black solid and dashed lines in panels **c**, **d** indicate iso-power contours.

instrumental in the discovery of the quantum-Hall effect[29], which led to the discovery of topological insulators[46] and introduced topology into condensed-matter physics[47]. Epitaxial integration of semiconductor/superconductor heterostructures could enable phenomena that require both materials families, such as the Majorana zero-modes for braiding-based, topologically protected quantum computation[11,48]. Moreover, the presence of spontaneous and piezoelectric polarization induced by broken inversion symmetry in group III/nitride semiconductor crystals[49] offers the possibility of Rashba-driven topological insulators[50]. In more near-term applications, NbN$_x$-based single-photon detectors can now be epitaxially integrated with GaN HEMT amplifiers for secure quantum communications. Finally, combining GaN HEMT microwave amplifiers with NbN$_x$-based Josephson junctions can provide an all-epitaxial platform for superconducting qubits whereby the most desirable properties of semiconductors and superconductors are combined epitaxially in a seamless braid.

Online Content Methods, along with any additional Extended Data display items and Source Data, are available in the online version of the paper; references unique to these sections appear only in the online paper.

1. Onnes, H. K. *Investigations into the Properties of Substances at Low Temperatures, Which Have Led, Amongst Other Things, to the Preparation of Liquid Helium.* (Nobel Lectures, 1913).
2. Riordan, M. & Hoddeson, L. in *Crystal Fire* 88–90 (WW Norton and Company, 1998).
3. Kroemer, H. Nobel lecture. Quasielectric fields and band offsets: teaching electrons new tricks. *Rev. Mod. Phys.* **73**, 783–793 (2001).
4. Alferov, Z. I. Nobel lecture. The double heterostructure concept and its applications in physics, electronics, and technology. *Rev. Mod. Phys.* **73**, 767–782 (2001).
5. Jena, D. Tunneling transistors based on graphene and 2-D crystals. *Proc. IEEE* **101**, 1585–1602 (2013).
6. Ladd, T. D. *et al.* Quantum computers. *Nature* **464**, 45–53 (2010).
7. Mooij, J. *et al.* Josephson persistent-current qubit. *Science* **285**, 1036–1039 (1999).
8. Lancaster, M. *et al.* Superconducting microwave resonators. In *IEE Proceedings H (Microwaves, Antennas and Propagation),* vol. 139, 149–156 (IET, 1992).
9. Cassidy, M. C. *et al.* Demonstration of an ac Josephson junction laser. *Science* **355**, 939–942 (2017).
10. Gol'tsman, G. N., Okunev, O., Chulkova, A., Lipatov, A., Semenov, K., Voronov, B. & Dzardanov, A. Picosecond superconducting single-photon optical detector. *Appl. Phys. Lett.* **79**, 705–707 (2001).
11. Mourik, V. *et al.* Signatures of Majorana fermions in hybrid superconductor-semiconductor nanowire devices. *Science* **336**, 1003–1007 (2012).
12. Sarma, S. D., Freedman, M. & Nayak, C. Majorana zero modes and topological quantum computation. *npj Quant. Information* **1**, 15001 (2015).
13. Krogstrup, P. *et al.* Epitaxy of semiconductor–superconductor nanowires. *Nat. Mater.* **14**, 400–406 (2015).
14. Yue, Y. *et al.* Ultrascaled InAlN/GaN high electron mobility transistors with cutoff frequency of 400 GHz. *Jpn. J. Appl. Phys.* **52**, 08JN14 (2013).
15. Li, W. *et al.* Polarization-engineered III-nitride heterojunction tunnel field-effect transistors. Exploratory solid-state computational devices and circuits. *IEEE J. Exp. Solid State Comp. Devices Circuits* **1**, 28–34 (2015).
16. Hu, Z. *et al.* Near unity ideality factor and Shockley-Read-Hall lifetime in GaN-on-GaN pn diodes with avalanche breakdown. *Appl. Phys. Lett.* **107**, 243501 (2015).
17. Islam, S. M. *et al.* MBE-grown 232–270 nm deep-UV LEDs using monolayer thin binary GaN/AlN quantum heterostructures. *Appl. Phys. Lett.* **110**, 041108 (2017).
18. Sheu, J.-K. *et al.* White-light emission from near UV InGaN-GaN LED chip precoated with blue/green/red phosphors. *IEEE Photonics Technol. Lett.* **15**, 18–20 (2003).

19. Dubois, M.-A. & Muller, C. in *MEMS-based Circuits and Systems for Wireless Communication* (eds Enz, C. C. & Kaiser, A.) 3–28 (Springer, 2013).
20. Pernice, W. H. *et al.* High-speed and high-efficiency travelling wave single-photon detectors embedded in nanophotonic circuits. *Nat. Commun.* **3,** 1325 (2012).
21. Faucher, M. *et al.* Niobium and niobium nitride SQUIDs based on anodized nanobridges made with an atomic force microscope. *Physica C* **368,** 211–217 (2002).
22. Song, S., Jin, B., Yang, H., Ketterson, J. & Schuller, I. K. Preparation of large area NbN/AlN/NbN Josephson junctions. *Jpn. J. Appl. Phys.* **26,** 1615 (1987).
23. Hajenius, M. *et al.* Low noise NbN superconducting hot electron bolometer mixers at 1.9 and 2.5 THz. *Supercond. Sci. Technol.* **17,** S224 (2004).
24. Eastman, L. F. & Mishra, U. K. The toughest transistor yet. *IEEE Spectr.* **39,** 28 (2002).
25. Katzer, D. S. *et al.* Epitaxial metallic β-Nb$_2$N films grown by MBE on hexagonal SiC substrates. *Appl. Phys. Exp.* **8,** 085501 (2015).
26. Meyer, D. J. *et al.* Epitaxial lift-off and transfer of III-N materials and devices from SiC substrates. *IEEE Trans. Semicond. Manuf.* **29,** 384–389 (2016).
27. Sanjinés, R., Benkahoul, M., Sandu, C., Schmid, P. & Lévy, F. Electronic states and physical properties of hexagonal β-Nb$_2$N and δ'-NbN nitrides. *Thin Solid Films* **494,** 190–195 (2006).
28. Meyer, D. J. *et al.* N-polar n+ GaN cap development for low ohmic contact resistance to inverted HEMTs. *Phys. Status Solidi C* **9,** 894–897 (2012).
29. Klitzing, K. v., Dorda, G. & Pepper, M. New method for high-accuracy determination of the fine-structure constant based on quantized Hall resistance. *Phys. Rev. Lett.* **45,** 494 (1980).
30. Xi, X. *et al.* Ising pairing in superconducting NbSe$_2$ atomic layers. *Nat. Phys.* **12,** 139–143 (2016).
31. Clogston, A. M. Upper limit for the critical field in hard superconductors. *Phys. Rev. Lett.* **9,** 266 (1962).
32. Nam, H. *et al.* Ultrathin two-dimensional superconductivity with strong spin–orbit coupling. *Proc. Natl Acad. Sci. USA* **113,** 10513–10517 (2016).
33. Kozuka, Y. *et al.* Two-dimensional normal-state quantum oscillations in a superconducting heterostructure. *Nature* **462,** 487–490 (2009).
34. Tinkham, M. Effect of fluxoid quantization on transitions of superconducting films. *Phys. Rev.* **129,** 2413 (1963).
35. Aoi, K., Meservey, R. & Tedrow, P. Hc (θ) and Tinkham's formula for high-field superconductors. *Phys. Rev. B* **7,** 554 (1973).
36. Ambacher, O. *et al.* Two-dimensional electron gases induced by spontaneous and piezoelectric polarization charges in N-and Ga-face AlGaN/GaN heterostructures. *J. Appl. Phys.* **85,** 3222–3233 (1999).
37. Jena, D. *et al.* Magnetotransport properties of a polarization-doped three-dimensional electron slab. *Phys. Rev. B* **67,** 153306 (2003).
38. Cao, Y., Wang, K., Orlov, A., Xing, H. & Jena, D. Very low sheet resistance and Shubnikov-de Haas oscillations in two-dimensional electron gases at ultrathin binary AlN/GaN heterojunctions. *Appl. Phys. Lett.* **92,** 152112 (2008).
39. Hamaguchi, C. *Basic Semiconductor Physics* (Springer, 2001).
40. Manfra, M. J. *et al.* Electron mobility exceeding 160 000 cm^2/Vs in AlGaN/GaN heterostructures grown by molecular-beam epitaxy. *Appl. Phys. Lett.* **85,** 5394–5396 (2004).
41. Dingle, R. Some magnetic properties of metals. II. The influence of collisions on the magnetic behaviour of large systems. *Proc. R. Soc. Lond. A* **211,** 517–525 (1952).
42. Jena, D. & Mishra, U. K. Quantum and classical scattering times due to charged dislocations in an impure electron gas. *Phys. Rev. B* **66,** 241307 (2002).
43. Hsu, J. *et al.* Effect of growth stoichiometry on the electrical activity of screw dislocations in GaN films grown by molecular-beam epitaxy. *Appl. Phys. Lett.* **78,** 3980–3982 (2001).
44. Kaun, S. W., Wong, M. H., Mishra, U. K. & Speck, J. S. Correlation between threading dislocation density and sheet resistance of AlGaN/AlN/GaN heterostructures grown by plasma-assisted molecular beam epitaxy. *Appl. Phys. Lett.* **100,** 262102 (2012).
45. Shukla, N. *et al.* A steep-slope transistor based on abrupt electronic phase transition. *Nat. Commun.* **6,** 7812 (2015).
46. Thouless, D. J., Kohmoto, M., Nightingale, M. P. & den Nijs, M. Quantized Hall conductance in a two-dimensional periodic potential. *Phys. Rev. Lett.* **49,** 405 (1982).
47. Hasan, M. Z. & Kane, C. L. Colloquium. Topological insulators. *Rev. Mod. Phys.* **82,** 3045–3067 (2010).
48. Beenakker, C. Search for Majorana Fermions in superconductors. *Annu. Rev. Condens. Matter Phys.* **4,** 113–136 (2013).
49. Wood, C. & Jena, D. *Polarization Effects in Semiconductors: From Ab-Initio Theory to Device Applications* (Springer, 2007).
50. Miao, M. S. *et al.* Polarization-driven topological insulator transition in a GaN/InN/GaN quantum well. *Phys. Rev. Lett.* **109,** 186803 (2012).

Author Contributions R.Y., S.V. and J.W. performed electrical, magnetic and magnetotransport measurements. D.S.K, N.N, B.P.D and D.J.M grew and characterized the epitaxial layers. Y.H. performed scanning transmission electron microscopy (STEM) analysis on thin NbN$_x$ films under the supervision of D.A.M. S.R. conducted the transmission electron microscopy (TEM) measurements. R.Y. and G.K. conducted experimental data analysis and theoretical calculations, with help from D.J. and H.G.X. R.Y., G.K. and D.J. wrote the manuscript, with input from all authors.

METHODS

We describe here in detail the epitaxial growth and structural, magnetic and electronic characterization of the group III/nitride semiconductor heterostructures and NbN$_x$ superconductors. We also describe the method of fabrication, as well as measurements and characterization, of the epitaxial semiconductor transistor/superconductor heterostructures and devices.

MBE growth. Epitaxial NbN$_x$ films were grown at 800 °C by radio-frequency plasma-assisted MBE on three-inch-diameter, metal-polar semi-insulating 4H- and 6H-SiC substrates. The substrates had been commercially polished using chemical–mechanical polishing to an epi-ready finish, and were used as received. The reactive nitrogen was generated using a radio-frequency plasma source fed by ultrahigh-purity N$_2$, which was further purified by an in-line purifier. The Nb flux was generated using an *in situ* electron-beam evaporator source with 3N5-pure (excluding tantalum, Ta) Nb pellets in a tungsten hearth liner. Further details regarding MBE growth conditions are in ref. 25.

Structural measurements. We measured the surface morphology of the MBE-grown NbN$_x$ films using a Bruker Dimension FastScan atomic force microscope in tapping mode. The root-mean-square roughness of the 5-nm NbN$_x$ film on SiC is 0.15 nm in an area of $3 \times 3 \mu m^2$, and 0.56 nm for the 35-nm film (Extended Data Fig. 2). We determined the lattice constants and phase of the NbN$_x$ films through X-ray diffraction (XRD) measurements, using a Rigaku system that employs a rotating copper anode to produce Cu-Kα radiation. Structural properties and lattice parameters of NbN$_x$ on SiC are given in ref. 51. The measured XRD spectra of the 5-nm and 35-nm films are shown in Extended Data Fig. 3: the peaks for NbN$_x$ are seen in first- and second-order reflection of the SiC (0004) plane in the relatively thick 35-nm sample, but the peaks are absent in the 5-nm sample because of the weak XRD signal in such thin films.

Transport and magnetic measurements. All of our electrical transport, Hall-effect and VSM measurements were carried out in a physical property measurement system (PPMS) manufactured by Quantum Design Inc. Extended Data Table 1 summarizes the basic material parameters extracted from measurements on the 5-nm and 35-nm samples. Extended Data Fig. 6 shows that, at 300 K, the carrier density in these NbN$_x$ films is as high as $n_{3d} \approx 10^{23}$ cm^{-3}, but the mobility is less than 1 cm^2 V^{-1}s^{-1}, probably limited by impurities, crystal defects and phonons. In terms of the superconducting behaviour, critical temperatures extracted from electrical resistance and VSM measurements are consistent with each other, but vary slightly from sample to sample in the range 6–15 K.

Characterization of the dependence of superconductivity on the in-plane magnetic field was limited by the 14 T field capabilities of our measurement system. We anticipate that our ongoing low-temperature and high-magnetic-field (up to 35 T) measurements will provide deeper insights into the orbital/spin pair-breaking mechanism and the presence of spin-orbit scattering.

Critical current density. Extended Data Fig. 6b, c shows the measured J_c in our MBE-grown NbN$_x$ films. We carried out the measurements by injecting current into the film and detecting the voltage drop when the injected current density exceeded J_c. The measured values are close to 10^5 A cm^{-2} for MBE-grown NbN$_x$.

Pair-breaking mechanisms in epitaxial thin NbN$_x$ films. The in-plane critical fields measured for the 5-nm NbN$_x$ epitaxial superconducting layers are much higher than expected from the out-of-plane critical fields and the Tinkham formula. Mechanisms that could lead to this phenomenon include a modified electron g-factor[31], the presence of spin-orbit scattering[52], and Rashba spin-orbit coupling[32].

If the mechanism were a modified electron g-factor, then given that the measured critical in-plane field is a factor of two larger than the Pauli limit, the epitaxial NbN$_x$ would need an effective g-factor of less than 1, which we find unlikely: because NbN$_x$ is a good metal, we suspect its effective g-factor to be close to 2 (ref. 53). Spin-orbit scattering is possible in the MBE-grown NbN$_x$ films owing to the presence of trace amounts of Ta in the purest available Nb sources. However, the dilute concentration of Ta that we have measured in our MBE NbN$_x$ suggests that this scenario is unlikely.

Finally, the presence of Rashba spin-splitting owing to broken inversion symmetry of the samples has recently been suggested[32] as a mechanism by which to suppress the Pauli paramagnetic limit. Because our films are grown in an asymmetric stack, we find this the most plausible explanation. Previous experimental and theoretical work has suggested the importance of Rashba spin-orbit coupling in identifying an anomalously large $H_{c2}^{\parallel}$. However, our epitaxial NbN$_x$ provides a platform for testing this idea directly, because of the ability to grow nominally symmetric stacks in NbN$_x$—a feat difficult in ultrathin lead films[32], but potentially possible, if challenging, in two-dimensional materials.

Shubnikov–de Haas oscillations. Extended Data Fig. 7a shows the raw measured Shubnikov–de Haas oscillations of the GaN/AlGaN 2DEG grown epitaxially on NbN$_x$ layers. The oscillations become sharper as the temperature is lowered. We

used these Shubnikov–de Haas measurements, with a fit to the Lifshitz–Kosevich form of the magnetoresistance, to extract carrier concentration, effective mass and quantum-scattering times as discussed in the main text. The magnetoresistance data were uniformly resampled over an inverse magnetic field, and then smoothed over a window of 0.00056 T^{-1} before background subtraction. To extract the effective mass and quantum-scattering times, we removed the non-oscillating background component of the resistance and used the oscillatory components (Extended Data Fig. 7a inset). A non-oscillatory background of the form $p(1/B) = a + b/B^{1/2} + c/B$ was subtracted from the R_{xx} data before fitting to the Lifshitz–Kosevich form.

Extended Data Fig. 7b shows a Landau plot of the Shubnikov–de Haas oscillation peaks. The range of magnetic fields used in this measurement, 0–14 T, allowed the Fermi level to fill 19–25 Landau levels at a fixed 2DEG density of $n_{2d} \approx 1.2 \times 10^{13}$ cm^{-2}.

Superconductor/semiconductor transistor devices. To fabricate the GaN HEMT structure (Extended Data Fig. 4a inset), we first grew 28-nm NbN$_x$ on a 6H-SiC substrate by MBE; this was followed by nucleation with 22 nm AlN, two-step application of a 1.3-μm GaN buffer layer, and then growth of 32-nm Al$_{0.4}$Ga$_{0.6}$N and 32-nm GaN channel at 700 °C. After the growth, ohmic contacts with Ti/Al/Ni/Au (20/100/10/50 nm) stacks were defined by optical lithography and electron-beam evaporation. Rapid thermal annealing at 850 °C produced ohmic contacts with a contact resistance of 0.4 Ω mm^{-1}. Inductively coupled plasma etching with a Cl$_2$/BCl$_3$/Ar gas was then used to isolate separate HEMTs. To reduce the gate leakage current, we deposited a 10-nm-thick, high-K dielectric layer of TiO$_2$ by atomic-layer deposition at 300 °C; this was followed by Pt/Au (30/200 nm) electron-beam evaporation to produce the gate metal stack. Finally, the TiO$_2$ on top of the drain and source contacts were removed with fluorine-based plasma etching, and a second metalization of Ti/Pt/Au (25/25/400 nm) was performed.

Using fabricated van der Pauw structures, we performed Hall-effect measurements on the 2DEG at the GaN/Al$_{0.4}$Ga$_{0.6}$N interface. We determined the electron concentration to be 1.3×10^{13} cm^{-2}, with a mobility of 1,350 cm^2 V^{-1} s^{-1} at room temperature and 3,400 cm^2 V^{-1} s^{-1} at 2 K, indicating that a high-quality 2DEG channel is achieved in these heterostructures and, more importantly, that processing did not lead to performance degradation.

A representative room-temperature electrical characterization of the fabricated GaN HEMTs on NbN$_x$ is shown in Extended Data Fig. 4. For a gate length of $L_g = 1 \mu$m and gate width of $W = 75 \mu$m, the transistors show an I_{on}/I_{off} ratio of more than 10^5 (Extended Data Fig. 4a). The on-current density exceeds 1 A mm^{-1} at $V_d = 3$ V and $V_g = -1$ V, with a clear current saturation (Extended Data Fig. 4b). Overall, the properties of the transistors studied here are similar to those of GaN HEMTs that are grown directly on SiC without the NbN$_x$ layer underneath[28]. This is, to our knowledge, the first successful direct epitaxial integration of a high-performance semiconductor transistor on a superconductor.

Extended Data Fig. 5 shows the measured drain currents without the superconductor load (J_{ds}; solid lines) and with the superconductor load ($J_{ds'}$; circles) at 5 K (less than T_c) under two different drain voltages in a linear scale. We can see that, when V_{ds} and $V_{ds'}$ are 0.1 V, the drain currents as a function of gate voltage are identical, because the NbN$_x$ remains superconducting with a resistance of 0 Ω throughout this gate-voltage range. However, when V_{ds} and $V_{ds'}$ are 1.1 V, the J_d versus $V_{gs'}$ curve deviates from the J_d versus V_{gs} curve once J_d exceeds 0.1 A mm^{-1}. This indicates the occurrence of a superconductor-to-metal phase transition of the NbN$_x$ film at the source end driven by this current (power) level.

Determination of N/Nb ratio (x) by SIMS. Extended Data Fig. 8 shows a SIMS measurement of the entire HEMT epitaxial heterostructure. Sharp and abrupt transitions of the SiC/superconductor, superconductor/AlN, AlN/GaN and AlGaN/GaN heterointerfaces are observed. The SIMS profile provides a calibrated measurement of the stoichiometry of each layer of the heterostructure. The semiconducting AlN, GaN and AlGaN layers are perfectly stoichimetric within the limits of the measurement, and the NbN$_x$ layer has an N/Nb ratio (x) of 43.3/56.7 = 0.762. Extended Data Table 2 shows additional N/Nb ratios measured by Rutherford back scattering (RBS) and SIMS, as well as the relation between N/Nb ratios, the residual resistance ratio (RRR) and the superconducting transition temperature.
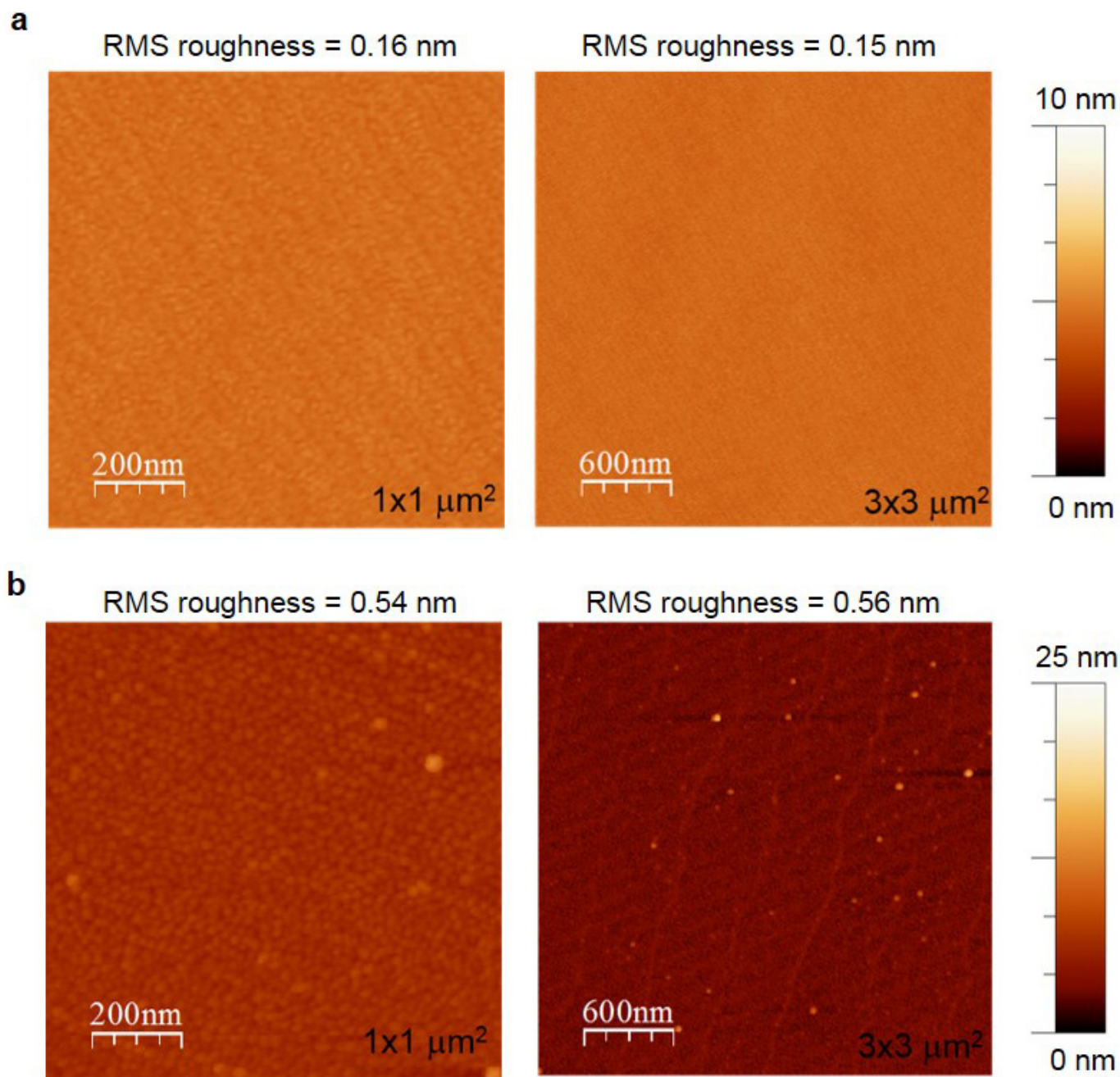
Data availability. The datasets generated and analysed here are available from the corresponding author on reasonable request.

51. Nepal, N. *et al.* Characterization of molecular beam epitaxy grown β-Nb$_2$N films and AlN/β-Nb$_2$N heterojunctions on 6H-SiC substrates. *Appl. Phys. Exp.* **9,** 021003 (2016).
52. Werthamer, N., Helfand, E. & Hohenberg, P. Temperature and purity dependence of the superconducting critical field H_{c2}. III. Electron spin and spin-orbit effects. *Phys. Rev.* **147,** 295 (1966).
53. MacDonald, A. Transition-metal g factor trends. *J. Phys. F* **12,** 2579 (1982).
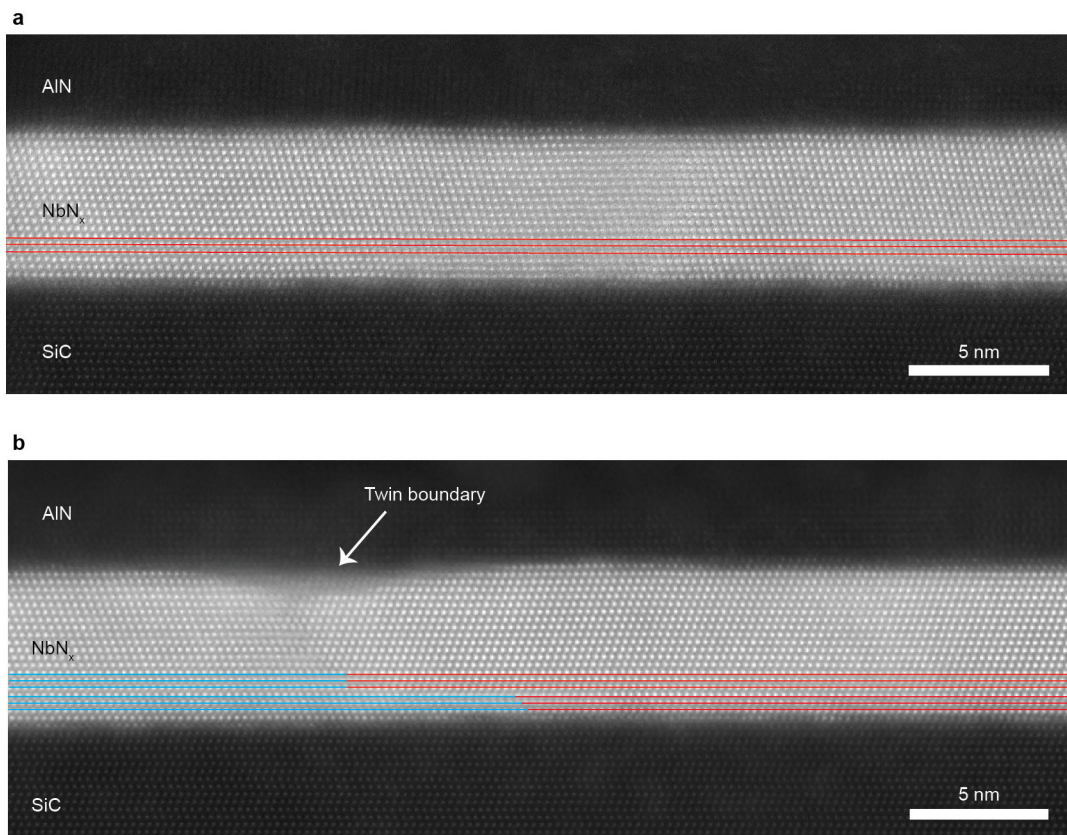
Extended Data Figure 1 | STEM of a large-area, MBE-grown AlN/NbN$_x$/ SiC heterostructure. a, STEM image of NbN$_x$/AlN grown on top of a SiC substrate, showing the single-crystal nature of NbN$_x$ over a large region. The red lines have been added as a guide to show the crystallinity across the entire range measured. **b**, A twin boundary and a stacking fault in the MBE NbN$_x$ layer. This STEM image of NbN$_x$/AlN on top of SiC shows a grain boundary with two cubic NbN$_x$ phases rotated across each other. The red and blue lines have been added to draw out the stacking fault seen near the twin boundary.

a

RMS roughness = 0.16 nm   RMS roughness = 0.15 nm

10 nm

200nm

1x1 µm²   600nm   3x3 µm²   0 nm

b

RMS roughness = 0.54 nm   RMS roughness = 0.56 nm

25 nm

200nm

1x1 µm²   600nm   3x3 µm²   0 nm

Extended Data Figure 2 | AFM characterizations of thin films. a, **b**, AFM images of epitaxial NbN_x films that are 5-nm thick (**a**) and 35-nm thick (**b**), over areas of $1 \times 1\,\mu m^2$ and $3 \times 3\,\mu m^2$. RMS, root mean squared.
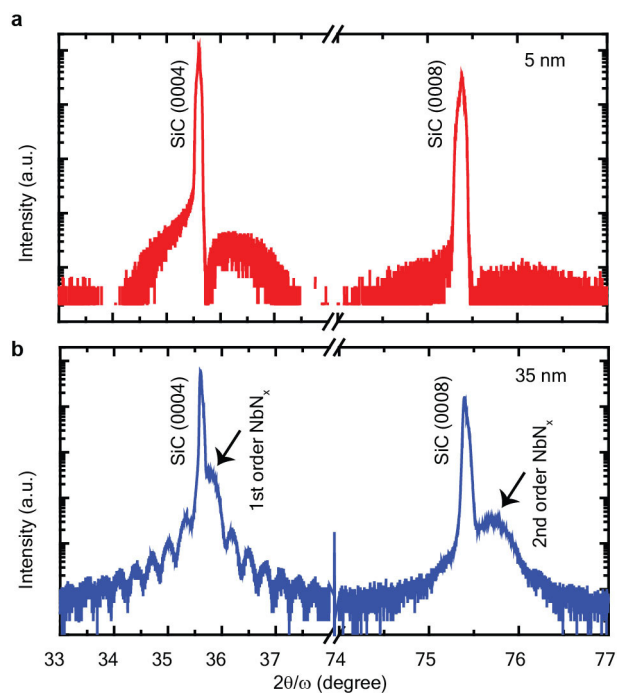
Extended Data Figure 3 | Symmetrical $2\theta/\omega$ XRD curves of 5-nm and 35-nm NbN$_x$ on 4H-SiC. 2θ is the angle between the incident and diffracted beams, and ω is the angle between the incident beam and the sample surface. **a**, The 5-nm sample. **b**, The 35-nm sample. There is a clear separation between the SiC and cubic NbN (first- and second-order) peaks in the 35-nm sample. But this feature is absent in the 5-nm sample, owing to the weak XDR signal intensity in such an ultrathin film.
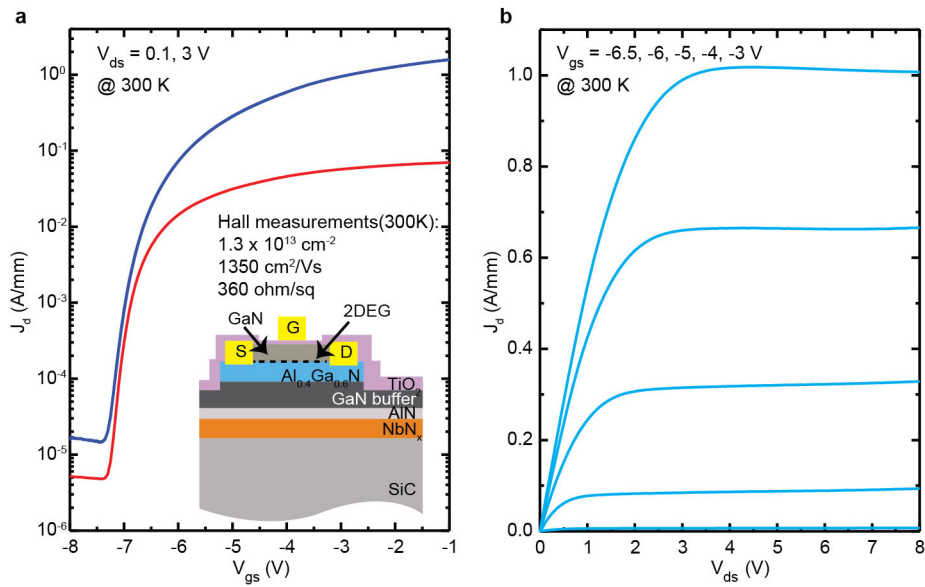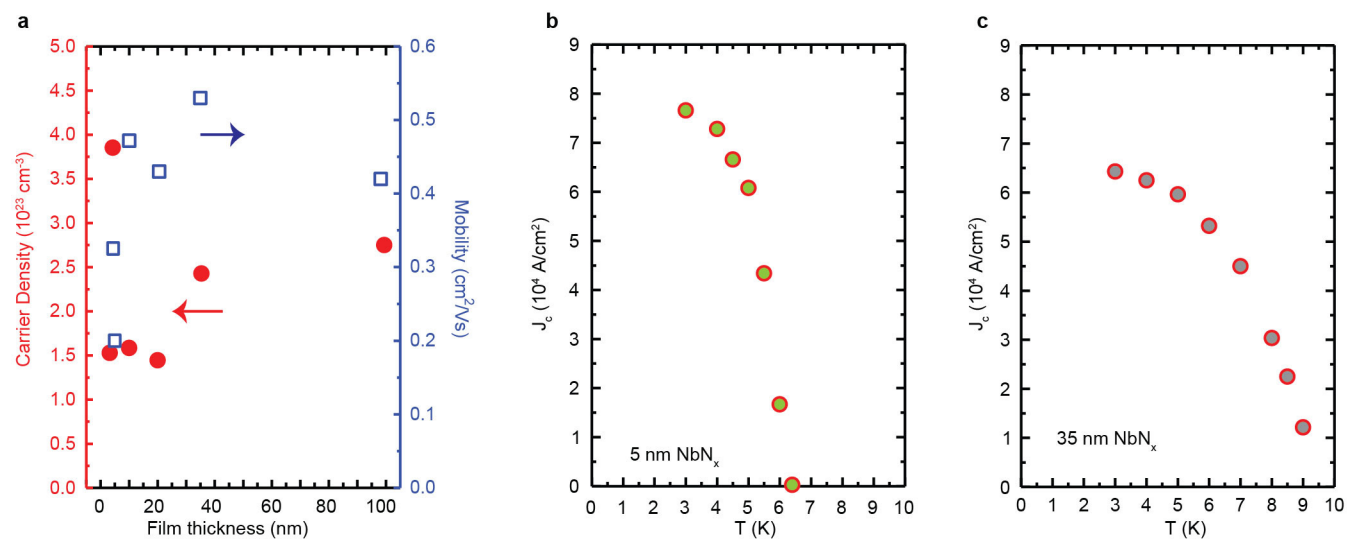
Extended Data Figure 4 | Electrical characterizations of HEMT structures. a, Drain current (J_d) versus top-gate voltage (V_{gs}) transfer curves at 300 K for HEMTs grown on NbN$_x$/SiC substrate, showing a high on/off ratio at source–drain voltages (V_{ds}) of 0.1 V (red curve) and 3 V (blue curve). **b**, J_d versus V_{ds} curves for various top-gate voltages (from bottom curve to top, −3 V, −4 V, −5 V, −6 V, −6.5 V) of GaN HEMTs at 300 K.
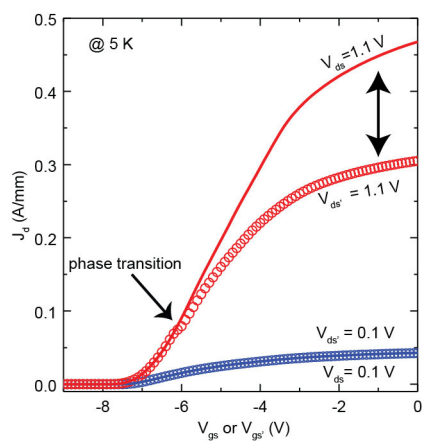
Extended Data Figure 5 | Representative transfer curves of a HEMT structure with superconducting load. The graph plots J_d versus V_{gs} (without superconductor load) and $V_{gs'}$ (with superconductor load) at 5 K, showing the phase transition of NbN_x that occurs when J_d is larger than 0.1 A mm^{-1}.

Extended Data Figure 6 | Electrical characterizations of superconducting NbN$_x$ films. a, Summary of carrier density and mobility for different thicknesses of NbN$_x$ films, ranging from 4 nm to 100 nm. The red arrow shows that the red dots correspond to the left-hand y axis; the blue squares correspond to the right-hand y axis. **b, c**, Critical current density as a function of temperature for 5-nm and 35-nm NbN$_x$ films.
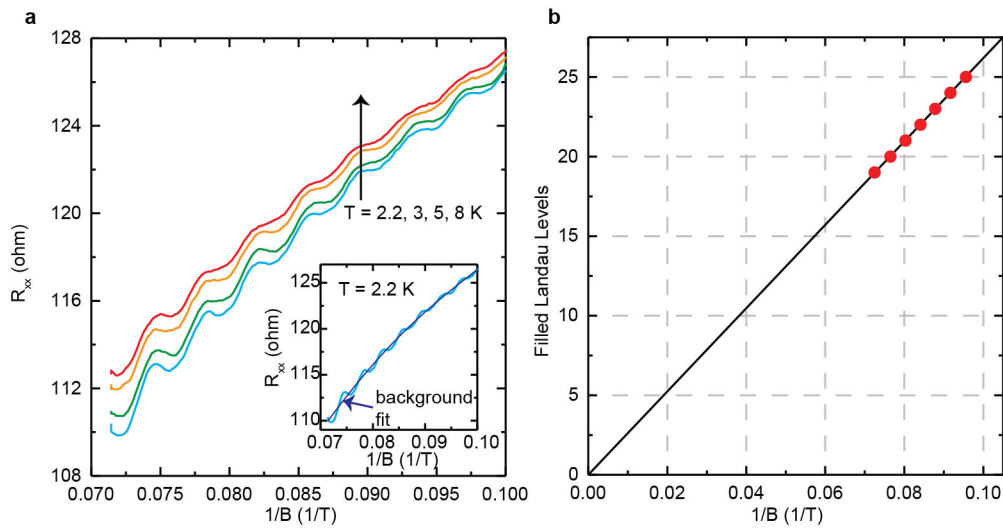
Extended Data Figure 7 | Shubnikov–de Haas oscillations of 2DEG.
a, Magnetoresistance (R_{xx}) plotted against inverse magnetic field ($1/B$) before background subtraction, taken over the magnetic-field range of 10 T to 14 T. The oscillations occur at periods of $1/B$—a clear indication of sharp peaks in the 2DEG density of states owing to Landau levels. The upward black arrow indicates increasing temperatures. The inset shows the 2.2 K data (light blue) with background (blue); the non-oscillating background was removed before evaluation of carrier concentration, effective mass, and scattering time. **b**, Landau plot of magnetoresistance relative minima plotted against inverse magnetic field. The slope of the line is $\hbar^2 \pi n_{SdH}/2m^*$; the density and effective mass are taken from the Lifshitz–Kosevich fit to magnetoresistance oscillations.
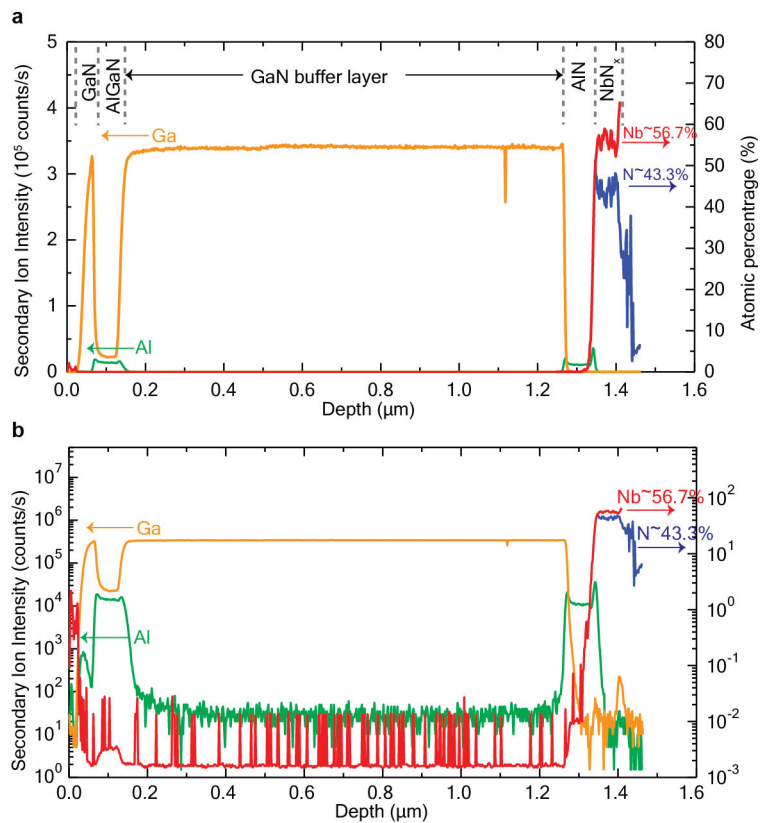
Extended Data Figure 8 | SIMS results obtained on the SiC/NbN$_x$/ AlN/GaN/AlGaN/GaN heterostructure. The left-hand y axis shows the secondary-ion intensity (counts per second) of Al and Ga atoms. The right-hand y axis indicates the atomic percentages of N and Nb atoms, which are respectively 43.3% and 56.7%, indicating a N/Nb ratio (x) of 0.762 in linear (**a**) and log (**b**) scale of signal intensity. The x axis denotes the depth of the sample from the top surface.

Extended Data Table 1 | Characteristic quantities in the normal state and superconducting state for thick and thin epitaxial NbN$_x$ films on 4H-SiC at 15 K

Qauntity	Symbol	Units	Thin Film	Thick Film
Film thicknness	d	nm	5	35
Sheet resistance	R_{sh}	Ω	107.9	9.8
Carrier concentration	n_{3d}	$10^{23}\ cm^{-3}$	2.14	2.29
Hall effect mobility	μ	cm^{-2}/Vs	0.54	0.93
Mean free path	l_{MFP}	Å	6.6	11.6
Tc (Resistance)	T_c	K	6.41	9.26
Tc (Magnetometry)	T_c	K	6.23	9.36
Coherence length	ξ	nm	10.56	10.06

Extended Data Table 2 | Epitaxial NbN$_x$ film properties

Sample	Thickness (nm)	RRR	T_c (K)	N/Nb ratio (x)	Notes
A	5	1.50	6.41	0.877 (RBS)	NbN$_x$ on SiC
B	35	1.86	9.26	0.751 (RBS)	NbN$_x$ on SiC
C	28	1.69	7.70	0.762 (SIMS)	GaN/AlGaN/GaN/AlN/NbN$_x$ on SiC

Film thickness, residual resistance ratio (RRR), superconducting critical temperature (T_c) and N/Nb ratio (x) are given for the samples discussed here. The film thickness was determined by RBS and TEM. RRR is defined as the ratios of the normal-state resistance at 300 K and at 20 K. T_c is identified as the midpoint of the superconducting transition. The N/Nb ratio x was measured by either RBS or SIMS.